48th AIAA Aerospace Sciences Meeting Including the New Horizons Forum and Aerospace Exposition
4 - 7 January 2010, Orlando, Florida

AIAA 2010-229

Low Re_m 3D MHD Hypersonic Equilibrium Flow Using High Order WENO Schemes

Jaejin Lee[*], Manuel A. Huerta[†], and Gecheng Zha[‡]University of Miami
Coral Gables, Florida 33124

We present work on 3D hypersonic laminar flows of air around blunt bodies with applied magnetic fields of various strengths. The air is heated by a shock that can change its thermodynamic properties. We treat the air both as a calorically perfect gas (chemically frozen) and as a real gas in thermodynamic equilibrium. Due to the high temperature the thermodynamic properties of the air are affected changes in specific heats due to rotational and vibrational excitation, by molecular dissociation, ionization, and other effects. We calculate the thermodynamic properties of the air using the curve fitting method implemented in the TGAS FORTRAN subroutines. The hot air is partially ionized, but the electrical conductivity of the air is low enough that we can use a low magnetic Reynolds number MHD model. Our numerical method is based on the Low Diffusion E-CUSP (LDE) scheme developed by Zha[1] et al with a 5th order WENO scheme.

I. Introduction

In this paper we continue our work beyond the results presented in our previous paper, Lee, Huerta, and Zha.[2] Hypersonic vehicles generate shocks that can heat the air sufficiently to partially ionize the air and create an electrically conducting plasma that can be studied using the equations of single fluid magnetohydrodynamics (MHD). Introducing strong applied magnetic and electric fields into the flow could have beneficial effects such as reducing heat damage, providing a sort of MHD parachute, and generating electric power or thrust in the vehicle. Among the many authors that have done numerical simulations of steady hypersonic MHD flows we mention here Bityurin, Lineberry, Potebnia, et. al.,[3] Bityurin and Bocharov,[4] Bityurin, Zeigarnik and Kuranov,[5] Fujino, Kondo and Ishikawa,[6] MacCormack,[7] and Hoffmann, Damevin, and Dietiker.[8] The low diffusion E-CUSP (LDE) scheme with a fifth order WENO scheme recently developed by Zha[1] et al. is very good in resolving flow fields with shock discontinuities. The purpose of this paper is to incorporate the low

---

[*] Graduate Student, Department of Physics

[†] Professor, Department of Physics, Senior AIAA Member

[‡] Associate Professor, Department of Mechanical and Aerospace Engineering, Senior AIAA Member

magnetic Reynolds number MHD model and the thermodynamics of high temperature air to the above CFD algorithm so that it can be used to simulate hypersonic flows with MHD effects. In this paper we compare results treating air as chemically frozen, neglecting all high temperature real gas effects, with results obtained treating the air as a real gas in thermodynamic equilibrium, whose thermodynamic properties are changed by the high temperature. Realistic flows are turbulent, but in this paper the Reynolds number is low, so we only show results for laminar flow.

II. Treatment of Real Gas Effects

The high temperature behind the hypersonic bow shock causes molecular dissociation, chemical reactions, ionization, and other effects that change the equation of state and the energy equation of the gas. A complete treatment of this requires the inclusion of reaction rate equations for each chemical species, the inclusion of rotational and vibrational energy equations, and other effects, possibly with the presence of two or even three distinct temperatures. Here we simply assume that there is enough time for the gas to reach local thermodynamic equilibrium, and we calculate the gas properties for air in chemical and thermodynamic equilibrium using the the curve fitting method implemented in the TGAS FORTRAN subroutines developed by Srinivasan, Tannehill, and Weilmuenster,[9] and Srinivasan, Tannehill, and Weilmuenster.[10] These subroutines give the pressure p and temperature T in terms of an equivalent ratio of specific heats $\tilde{\gamma}$ in the form

$$\tilde{\gamma} = \tilde{\gamma}(e_{int}, \rho), \quad p = \rho e_{int}(\tilde{\gamma} - 1), \quad T = T(p, \rho), \tag{1}$$

where ρ and e_{int} are the gas density and specific internal energy. In this abstract we use Sutherland's law to calculate the viscosity μ, and we take the electrical conductivity to be constant in those parts of the flow that exceed a threshold temperature.

III. The MHD Model

Single-fluid magnetohydrodynamics (MHD) describes an electrically conducting but electrically neutral fluid of density ρ, velocity $\mathbf{u}$, pressure p, energy per unit mass e, viscosity tensor $\bar{\bar{\tau}}$, and heat flux vector $\mathbf{q}$. The electrical quantities are the magnetic field $\mathbf{B}$, the electric field $\mathbf{E}$, the current density $\mathbf{J}$, and the electrical conductivity σ, which may be a scalar or a tensor, depending on the model. In principle σ should be calculated from an air chemistry model, such as in Ref. [7], but in this abstract we assume that σ is given, and we do not discuss the air chemistry. The plasma is taken to obey Ohm's law

$$\mathbf{J} = \sigma(\mathbf{E} + \mathbf{u} \times \mathbf{B}). \tag{2}$$

The magnetic field is advanced in time using Faraday's law

$$\frac{\partial \mathbf{B}}{\partial t} = -\nabla \times \mathbf{E}. \tag{3}$$

The Ampère-Maxwell equation, which could be used to advance $\mathbf{E}$ is

$$\mu_0 \epsilon_0 \frac{\partial \mathbf{E}}{\partial t} = \nabla \times \mathbf{B} - \mu_0 \mathbf{J}. \tag{4}$$

However, MHD describes low frequency phenomena, in which the conduction current is much greater than the displacement current, that is,

$$\mathbf{J} \gg \epsilon_0 \frac{\partial \mathbf{E}}{\partial t}. \tag{5}$$

The displacement current is therefore neglected and we use the pre-Maxwell equation

$$\mu_0 \mathbf{J} = \nabla \times \mathbf{B}, \tag{6}$$

which gives $\mathbf{J}$ in terms of $\mathbf{B}$. This means that $\mathbf{E}$ is not advanced in time, but is obtained in terms of $\mathbf{B}$ using Eqs. [2] and [6]. As a consequence of this, MHD cannot describe the usual type of high frequency electromagnetic waves. However, MHD does describe three interesting types of waves known as the Alfvén wave and the fast and slow magneto-acoustic waves. $\mathbf{E}$ can be eliminated from Eq.(3) and we rewrite it as

$$\frac{\partial \mathbf{B}}{\partial t} = -\nabla \times (\frac{\mathbf{J}}{\sigma} - \mathbf{u} \times \mathbf{B}) = \nabla \times (\mathbf{u} \times \mathbf{B}) + \frac{1}{\mu_0 \sigma} \nabla^2 \mathbf{B}, \tag{7}$$

which is the equation that advances $\mathbf{B}$ in time, and can be written in conservation form as

$$\frac{\partial \mathbf{B}}{\partial t} + \nabla \cdot (\mathbf{u} \otimes \mathbf{B} - \mathbf{B} \otimes \mathbf{u}) = \frac{1}{\mu_0 \sigma} \nabla^2 \mathbf{B}. \tag{8}$$

The fluid quantities $\rho, \mathbf{u}$, and e are advanced in time using the usual conservation of mass,

$$\frac{\partial \rho}{\partial t} + \nabla \cdot (\rho \mathbf{u}) = 0, \tag{9}$$

conservation of momentum,

$$\frac{\partial (\rho \mathbf{u})}{\partial t} + \nabla \cdot (\rho \mathbf{u} \otimes \mathbf{u}) = -\nabla p + \nabla \cdot \bar{\bar{\tau}} + \mathbf{J} \times \mathbf{B}, \tag{10}$$

which now includes the magnetic force density $\mathbf{J} \times \mathbf{B}$, and finally e is advanced with the equation of conservation of energy,

$$\frac{\partial}{\partial t}(\rho e) + \nabla \cdot \Big[(\rho e + p)\mathbf{u}\Big] = -\nabla \cdot \mathbf{q} + \nabla \cdot (\bar{\bar{\tau}} \cdot \mathbf{u}) + \mathbf{E} \cdot \mathbf{J}. \tag{11}$$

This equation is rewritten using Eq. [2] as

$$\frac{\partial}{\partial t}(\rho e) + \nabla \cdot \Big[(\rho e + p)\mathbf{u}\Big] = -\nabla \cdot \mathbf{q} + \nabla \cdot (\bar{\bar{\tau}} \cdot \mathbf{u}) + \frac{J^2}{\sigma} + (\mathbf{J} \times \mathbf{B}) \cdot \mathbf{u}. \tag{12}$$

The system is closed by giving appropriate expressions for $e, \bar{\bar{\tau}}, \mathbf{q}$, and σ in terms of the other quantities. The specific energy e is given by

$$e = e_{int} + \frac{1}{2} u^2, \tag{13}$$

and the pressure is obtained using

$$e_{int} = \frac{p}{(\tilde{\gamma} - 1)\rho}, \tag{14}$$

where e_{int} is advanced using Eq. [12], and $\tilde{\gamma}$, which equals 1.4 for chemically frozen air, is calculated using Eqs. [1] from the curve fitting method for air in chemical and thermodynamic equilibrium. In Eqs. [10], [11] and [12], $\mathbf{J}$ can be eliminated using Eq. [2].

IV. The Full MHD Model and the Low Magnetic Reynolds Number Approximation

The flow around a hypersonic vehicle causes a bow shock that heats the air enough to give it some electrical conductivity. We are interested in describing steady hypersonic flow around a vehicle that carries a magnet that applies a strong steady magnetic field $\mathbf{B}_a$ to the flow with the intention of reducing surface heating and increasing the drag force in a sort of MHD parachute. The drag force increases because the integral of $\mathbf{J} \times \mathbf{B}$ over the fluid volume appears as a reaction force on the magnet. In this paper we have not included a calculation of this reaction force. The vehicle may also have conductors on its surface arranged so as to generate electrical power by extracting energy from the flow. The vehicle might also have a steady source of $\mathcal{E}$mf, $\mathcal{E}_a$, and apply a strong electric field $\mathbf{E}_a$, such as in a nozzle, to produce MHD thrust. We think of $\mathbf{B}_a$ and $\mathbf{E}_a$ as independent of time in the reference frame of the vehicle. The total magnetic and electric fields in the plasma, $\mathbf{B} = \mathbf{B}_a + \mathbf{B}_i$ and $\mathbf{E} = \mathbf{E}_a + \mathbf{E}_i$ are the sum of the applied and induced fields. The applied fields have zero divergence and curl inside the flow field.

The full MHD model presented in Section III advances in time the eight-dimensional flux vector $[\rho, \rho u, \rho v, \rho w, B_x, B_y, B_z, \rho e_t]$, where $u, v,$ and w are the $x, y,$ and z components of $\mathbf{u}$, using Eqs. [9], [10], [12], and [8] in conservation form. The full MHD 8-dimensional problem is conceptually clear, because only the magnetic field is advanced in time. The current $\mathbf{J}$ is obtained from the magnetic field using Eq. [6]. Finally the electric field is calculated using the boundary conditions, knowing its curl from Eq. [3], and its divergence from requiring that Eq. [2] be compatible with $\nabla \cdot \mathbf{J} = 0$. Several authors have treated the full 8-dimensional problem. For example, a nozzle problem with a generator section to extract power from the incoming flow, and an accelerator section to produce thrust, using a tensor conductivity was treated in Ref. [7]. Ref. [8] also used the full 8-dimensional MHD model to treat flows around a flat plate and around a blunt body with zero electric field.

The ionized air produced in the hypersonic flow is a poor electrical conductor. Therefore the electrical current $\mathbf{J}$ induced in the plasma is small. The magnetic field $\mathbf{B}_i$ generated by the plasma current is much smaller than the applied field, and diffuses in a fast time scale, which complicates the numerical simulations. This allows the use of a low magnetic Reynolds number approximation. When expressed in dimensionless variables, the electrical conductivity σ enters the problem via the magnetic Reynolds number

$$Re_m = \mu_0 \sigma U_{ref} L_{ref}, \tag{15}$$

where U_{ref} and L_{ref} are appropriate reference values of speed and length in the problem. When Re_m is small it is possible to treat the problem in a low Re_m approximation, which neglects the fields $\mathbf{B}_i$ and $\mathbf{E}_i$ induced by the plasma. In this model only the five fluid quantities in the five-dimensional flux vector $[\rho, \rho u, \rho v, \rho w, \rho e]$ need to be advanced in time using Eqs.[9], [10], and [12], with MHD source terms proportional to $\mathbf{J}$. Refs. [3] - [6] used the low Re_m approximation to study interesting effects, such as the MHD parachute and MHD power generation. MacCormack[11] showed that the full MHD solution agrees with the low Re_m solution for flow in a thrust producing nozzle for $Re_m = 0.17$. Damevin and Hoffmann[?] compared the full MHD solution including air chemistry with the low Re_m approximation in flows over a hemisphere and a cylinder. Khan, Hoffmann and Dietiker[12] used the full MHD model to treat flows with zero electric field around a flat plate and a blunt body and tested for agreement between the solutions of the full MHD model and the low Re_m approximation. They obtained good agreement for values of $Re_m < 0.125$.

To understand the validity of the low Re_m approximation we can think in terms of a sort of singular expansion in the small parameter Re_m. From Eq. [2] we see that the current is proportional to σ, so $\mathbf{J}$ is $O(Re_m)$, and from Eq. [6] we see that $\mathbf{B}_i$ is also $O(Re_m)$. The $1/(\mu_0\sigma)$ term in Eq. [7] does not change the order of $\mathbf{B}_i$, but rather it makes $\mathbf{B}_i$ diffuse in a short time scale, which complicates the numerical simulations. There are at least two time scales in the problem. First, we have $t_U = L_{ref}/U_{ref}$. There is also a magnetic diffusion fast time scale, $t_D = t_U * Re_m \ll t_U$. Then there are two dimensionless times $t_1^* = t/t_U$ and $t_2^* = t/t_D$. The field $\mathbf{B}_i$ depends on the two dimensionless times, $\mathbf{B}_i(t, \mathbf{R}) = \mathbf{B}_i(t_1^*, t_2^*, \mathbf{R})$. Then the derivative of $\mathbf{B}_i$ with respect to time looks like

$$\frac{\partial \mathbf{B}_i}{\partial t} = \frac{\partial \mathbf{B}_i}{\partial t_1^*}\frac{\partial t_1^*}{\partial t} + \frac{\partial \mathbf{B}_i}{\partial t_2^*}\frac{\partial t_2^*}{\partial t} = \frac{\partial \mathbf{B}_i}{\partial t_1^*}\frac{1}{t_U} + \frac{\partial \mathbf{B}_i}{\partial t_2^*}\frac{1}{t_D} = \frac{1}{t_U}\Big(\frac{\partial \mathbf{B}_i}{\partial t_1^*} + \frac{\partial \mathbf{B}_i}{\partial t_2^*}\frac{1}{Re_m}\Big). \tag{16}$$

The last term in Eq. [16] is balanced against the $1/(\mu_0\sigma)$ in Eq. [7], and $\mathbf{B}_i$ remains of $O(Re_m)$. A formal power series expansion of $\mathbf{J}$ and $\mathbf{B}$ in powers of Re_m would be

$$\mathbf{J} = Re_m \mathbf{J}^{(1)}(t_1^*) + Re_m^2 \mathbf{J}^{(2)}(t_i^*, t_2^*) + ..., \quad \mathbf{B}_i = Re_m \mathbf{B}_i^{(1)}(t_1^*) + Re_m^2 \mathbf{B}_i^{(2)}(t_1^*, t_2^*) + ... \tag{17}$$

Therefore the source terms in Eqs. [9], [10], and [12] are accurately kept through order $O(Re_m)$ by writing

$$\mathbf{J} \times \mathbf{B} \approx \mathbf{J} \times \mathbf{B}_a, \quad \text{where} \quad \nabla \times \mathbf{B}_a = 0. \tag{18}$$

In contrast to the full MHD model, where one would use Eq. [6] to get $\mathbf{J}$ from $\mathbf{B}_i$, in the low Re_m approximation we must use Ohm's law Eq. [2], which to lowest order becomes

$$\mathbf{J} \approx \sigma(\mathbf{E}^{(0)} + \mathbf{u} \times \mathbf{B}_a) \equiv Re_m \mathbf{J}^{(1)}. \tag{19}$$

But there still remains the problem of determining what is the lowest order electric field $\mathbf{E}^{(0)}$. From Eq. [3] we see that $\nabla \times \mathbf{E} = O(Re_m)$, therefore we take $\mathbf{E}^{(0)} = -\nabla\phi^{(0)}$. From Eq. [6] we see that $\nabla \cdot \mathbf{J} = 0$ to all orders in Re_m, so that Eq. [19] gives

$$\nabla^2\phi^{(0)} = -\nabla \cdot (\mathbf{u} \times \mathbf{B}_a) - (-\nabla\phi^{(0)} + \mathbf{u} \times \mathbf{B}_a) \cdot \Big(\frac{\nabla\sigma}{\sigma}\Big), \tag{20}$$

which must be solved subject to the appropriate boundary conditions. So, in general, one must solve this elliptic equation at each time step to get $\mathbf{J}$ from $\mathbf{E}^{(0)}$, and use that to advance $\mathbf{u}$ and ρe. The above expansions are not quite the same as doing a formal power series expansion in Re_m because in the low Re_m approximation the fluid quantities $\mathbf{u}, \rho, p$, etc. are

$$\mathbf{u} = \mathbf{u}^{(0)} + Re_m \mathbf{u}^{(1)}, \quad \rho = \rho^{(0)} + Re_m \rho^{(1)} \quad p = p^{(0)} + Re_m p^{(1)}. \tag{21}$$

The order $O(Re_m)$ terms are kept in the fluid quantities in order to see the plasma effects upon things like the location and strength of shocks. The orders of things are somewhat mixed up because what we called $\phi^{(0)}$ in Eq. [20] contains $\mathbf{u}$, which contains effects of $O(Re_m)$. Fortunately there are interesting problems in which the electric field is simple. In a problem of three dimensional flow with cylindrical symmetry, where $u_\pi = B_\phi = 0$ and $\partial/\partial\phi = 0$, Eq. [6] implies that $\mathbf{J} = J_\phi(r, z)\hat{\mathbf{e}}_\phi$, and Eqs. [2] and [3] imply that $\mathbf{E}^{(0)} =$

$E_\phi^{(0)}(r,z)\hat{\mathbf{e}}_\phi = 0$, as in Tomoyuki.[13] In the problem of two dimensional steady flow past a flat plate treated in Khan,[12] $u_z = B_z = 0$ and $\partial/\partial z = 0$. Then one has a current in the ignorable direction $J_z(x,y)$, and the electric field can be taken as $\mathbf{E} = 0$ if the current has a return path of zero resistance outside the plasma. Say that the plasma has a length L_z in the z direction. If the current has a return path located outside the plasma of resistance R, the voltage across the plasma will be $V = iR = E_z L_z$, where the total current i is

$$i = \int Jz dx dy = \int \sigma(\mathbf{u}\times\mathbf{B})_z dx dy. \tag{22}$$

If the return path not only has a resistance R, but also an applied emf $\mathcal{E}_a$ acting in the opposite direction of $(\mathbf{u}\times\mathbf{B})_z$, then the electric field in the plasma would be the constant field

$$\mathbf{E} = -\frac{\mathcal{E}_a + iR}{L_z}\hat{\mathbf{z}}. \tag{23}$$

V. The Governing Equations of a Three-dimensional Low Re_m Approximation

We use a generalized coordinate system

$$\xi(x,y,z), \quad \eta(x,y,z), \quad \zeta(x,y,z) \quad \text{with} \quad J_a = \frac{\partial(\xi,\eta,\zeta)}{\partial(x,y,z)}, \tag{24}$$

where J_a is the Jacobian determinant of the transformation of variables. We use the low diffusion E-CUSP (LDE) scheme developed by Zha, Shen, and Wang.[1] The governing equations are the laminar 3D Navier - Stokes equations due to the low reynolds number. Eqs.[9], [10], and [12] are as follows. In this abstract we only treat laminar flow. In the future we will include the Baldwin - Lomax turbulence model.

$$\frac{\partial Q}{\partial t} + \frac{\partial \mathbf{E}}{\partial \xi} + \frac{\partial \mathbf{F}}{\partial \eta} + \frac{\partial \mathbf{G}}{\partial \zeta} = \frac{1}{Re}\left(\frac{\partial \mathbf{R}}{\partial \xi} + \frac{\partial \mathbf{S}}{\partial \eta} + \frac{\partial \mathbf{T}}{\partial \zeta}\right) + \mathbf{S}_{MHD}. \tag{25}$$

The flux vector is

$$Q = \frac{1}{J_a}[\ \rho, \quad \rho u, \quad \rho v, \quad \rho w, \quad \rho e\ ]^T, \quad \text{where} \quad \rho e = \frac{p}{(\gamma-1)} + \frac{1}{2}(u^2+v^2+w^2), \tag{26}$$

and where u, v and w are the x, y and z components of the fluid velocity. The vector $\mathbf{S}_{MHD}$ contains the MHD source terms,

$$\mathbf{S}_{MHD} = \frac{1}{J_a}[\ 0, \quad (\mathbf{J}\times\mathbf{B}_a)_x, \quad (\mathbf{J}\times\mathbf{B}_a)_y, \quad (\mathbf{J}\times\mathbf{B}_a)_z, \quad \mathbf{E}\cdot\mathbf{J}\ ]^T \tag{27}$$

where

$$\mathbf{J} = \sigma(\mathbf{E} + \mathbf{u}\times\mathbf{B}_a), \tag{28}$$

and $\mathbf{E} = -\nabla\phi^{(0)}$ is determined by solving Eq. [20] at each time step using the boundary conditions. We note that $\mathbf{E}\cdot\mathbf{J}$ can be rewritten as

$$\mathbf{E}\cdot\mathbf{J} = \frac{\mathbf{J}\cdot\mathbf{J}}{\sigma} + (\mathbf{J}\times\mathbf{B}_a)\cdot\mathbf{u}. \tag{29}$$

However, in the geometries we treat here, the electric field is actually zero. We introduce the vectors **l**, **m**, **n**. These are the normal vectors on ξ, η, ζ surfaces with their magnitudes equal to the elemental surface area and pointing to the directions of increasing ξ, η, ζ,

$$\mathbf{l} = \frac{\nabla\xi}{J_a}\Delta\eta\Delta\zeta,\ \mathbf{m} = \frac{\nabla\eta}{J_a}\Delta\xi\Delta\zeta,\ \mathbf{n} = \frac{\nabla\zeta}{J_a}\Delta\xi\Delta\eta. \tag{30}$$

l_t, m_t, n_t stand for the grid moving velocities and are defined as

$$l_t = \frac{\xi_t}{J_a}\Delta\eta\Delta\zeta,\ m_t = \frac{\eta_t}{J_a}\Delta\xi\Delta\zeta,\ n_t = \frac{\zeta_t}{J_a}\Delta\xi\Delta\eta \tag{31}$$

When the grid is stationary, $l_t = m_t = z_t = 0$. Since $\Delta\xi = \Delta\eta = \Delta\zeta = 1$ in the current discretization, Eqs.(30) and (31) are written as the following in the solver,

$$\mathbf{l} = \frac{\nabla\xi}{J_a},\ \mathbf{m} = \frac{\nabla\eta}{J_a},\ \mathbf{n} = \frac{\nabla\zeta}{J_a}, \tag{32}$$

and

$$l_t = \frac{\xi_t}{J_a},\ m_t = \frac{\eta_t}{J_a},\ n_t = \frac{\zeta_t}{J_a}. \tag{33}$$

The matrices **E**, **F**, and **G** are

$$\mathbf{E} = \begin{bmatrix} \rho U \\ \rho u U + l_x p \\ \rho v U + l_y p \\ \rho w U + l_z p \\ (\rho e + p)\, U - l_t p \end{bmatrix},\ \mathbf{F} = \begin{bmatrix} \rho V \\ \rho u V + m_x p \\ \rho v V + m_y p \\ \rho w V + m_z p \\ (\rho e + p)\, V - m_t p \end{bmatrix},\ \mathbf{G} = \begin{bmatrix} \rho W \\ \rho u W + n_x p \\ \rho v W + n_y p \\ \rho w W + n_z p \\ (\rho e + p)\, W - n_t p \end{bmatrix}. \tag{34}$$

In the equations above, U, V and W are the contravariant velocities in the ξ, η and ζ directions,

$$\begin{aligned} U &= l_t + \mathbf{l}\cdot\mathbf{V} = l_t + l_x u + l_y v + l_z w \\ V &= m_t + \mathbf{m}\cdot\mathbf{V} = m_t + m_x u + m_y v + m_z w \\ W &= n_t + \mathbf{n}\cdot\mathbf{V} = n_t + n_x u + n_y v + n_z w, \end{aligned} \tag{35}$$

where $\mathbf{V} = (u, v, w)$ is the velocity vector. The viscosity and heat conduction flux vectors $\mathbf{R}, \mathbf{S}$, and $\mathbf{T}$ are

$$\mathbf{R} = \begin{bmatrix} 0 \\ l_k\tau_{xk} \\ l_k\tau_{yk} \\ l_k\tau_{zk} \\ l_k\beta_k \end{bmatrix},\ \mathbf{S} = \begin{bmatrix} 0 \\ m_k\tau_{xk} \\ m_k\tau_{yk} \\ m_k\tau_{zk} \\ m_k\beta_k \end{bmatrix},\ \mathbf{T} = \begin{bmatrix} 0 \\ n_k\tau_{xk} \\ n_k\tau_{yk} \\ n_k\tau_{zk} \\ n_k\beta_k \end{bmatrix}, \tag{36}$$

where

$$\beta_k = u_i\tau_{ki} - q_k. \tag{37}$$

The shear-stress τ_{ik} and total heat flux q_k in Cartesian Coordinate can be expressed as

$$\tau_{ik} = \mu\left[\left(\frac{\partial u_i}{\partial x_k} + \frac{\partial u_k}{\partial x_i}\right) - \frac{2}{3}\delta_{ik}\frac{\partial u_j}{\partial x_j}\right], \quad \text{and} \tag{38}$$

$$q_k = -\left(\frac{\mu}{Pr}\right)\frac{\partial T}{\partial x_k} \tag{39}$$

where, Pr is the Prandtl number, and μ is the molecular viscosity determined by Sutherland's law. In eqs.(36), (37), (38) and (39), the repeated subscripts i or k represent the coordinates x, y and z following the Einstein summation convention. Eqs.(38) and (39) are transformed to the generalized coordinate system in the computation.

VI. The Numerical Scheme

The inviscid fluxes are evaluated using the LDE scheme of Ref. [1] and the fifth order WENO scheme given below. The viscous terms are discretized using a 2nd order central differencing scheme.

VI.A. The Low Diffusion E-CUSP (LDE) Scheme

The basic idea of the E-CUSP scheme is to split the inviscid flux into the convective flux E^c and the pressure flux E^p. In a generalized coordinate system, the flux $\mathbf{E}$ can be split as follows

$$\mathbf{E} = E^c + E^p = \begin{pmatrix} \rho U \\ \rho u U \\ \rho v U \\ \rho w U \\ \rho e U \end{pmatrix} + \begin{pmatrix} 0 \\ l_x p \\ l_y p \\ l_z p \\ p\overline{U} \end{pmatrix}, \quad \text{where} \quad \overline{U} = l_x u + l_y v + l_z w. \tag{40}$$

The convective term, E^c is evaluated following the Edward's H-CUSP (enthalpy-CUSP) LDFSS[14, 15](low-diffusion-flux-splitting-scheme) ,

$$E^c = \rho U \begin{pmatrix} 1 \\ u \\ v \\ w \\ e \end{pmatrix} = \rho U f^c, \; f^c = \begin{pmatrix} 1 \\ u \\ v \\ w \\ e \end{pmatrix}. \tag{41}$$

Let

$$C = c\left(l_x^2 + l_y^2 + l_z^2\right)^{\frac{1}{2}} \tag{42}$$

where $c = \sqrt{\gamma R T}$ is the speed of sound. Then the convective flux at interface $\frac{1}{2}$ is evaluated as:

$$E^c_{\frac{1}{2}} = C_{\frac{1}{2}}\left[\rho_L C^+ f^c_L + \rho_R C^- f^c_R\right], \tag{43}$$

where, the subscripts L and R represent the left and right hand sides of the interface.

The interface speed of sound is

$$C_{\frac{1}{2}} = \frac{1}{2}\left(C_L + C_R\right). \tag{44}$$

The following relations are borrowed from Edwards LDFFS scheme[14,15] to express the formulations from $-\infty < M < \infty$,

$$\begin{aligned}
&C^{+} = \alpha_L^{+}\left(1+\beta_L\right)M_L - \beta_L M_L^{+} - M_{\frac{1}{2}}^{+}, \quad C^{-} = \alpha_R^{-}\left(1+\beta_R\right)M_R - \beta_R M_R^{-} + M_{\frac{1}{2}}^{-},\\
&M_L = \tfrac{U_L}{C_{\frac{1}{2}}}, \quad M_R = \tfrac{U_R}{C_{\frac{1}{2}}}, \quad \alpha_{L,R} = \tfrac{1}{2}\left[1 \pm sign\left(M_{L,R}\right)\right], \quad \beta_{L,R} = -max\left[0, 1 - int\left(\left|M_{L,R}\right|\right)\right],\\
&M_{\frac{1}{2}}^{+} = M_{\frac{1}{2}}\tfrac{C_R + C_L\Phi}{C_R + C_L}, \quad M_{\frac{1}{2}}^{-} = M_{\frac{1}{2}}\tfrac{C_L + C_R\Phi^{-1}}{C_R + C_L}, \quad \Phi = \tfrac{\left(\rho C^2\right)_R}{\left(\rho C^2\right)_L}, \quad M_{\frac{1}{2}} = \beta_L\delta^{+}M_L^{-} - \beta_R\delta^{-}M_R^{+},\\
&M_{L,R}^{\pm} = \pm\tfrac{1}{4}\left(M_{L,R} \pm 1\right)^2, \quad \text{and} \quad \delta^{\pm} = \tfrac{1}{2}\left\{1 \pm sign\left[\tfrac{1}{2}\left(M_L + M_R\right)\right]\right\}.
\end{aligned} \tag{45}$$

The pressure flux, E^p is evaluated as

$$E_{\frac{1}{2}}^{p} = \begin{pmatrix} 0 \\ p\,l_x \\ p\,l_y \\ p\,l_z \\ p\overline{U} \end{pmatrix} = \begin{pmatrix} 0 \\ \left(\mathcal{D}_L^{+}p_L + \mathcal{D}_R^{-}p_R\right)l_x \\ \left(\mathcal{D}_L^{+}p_L + \mathcal{D}_R^{-}p_R\right)l_y \\ \left(\mathcal{D}_L^{+}p_L + \mathcal{D}_R^{-}p_R\right)l_z \\ \overline{C}_{\frac{1}{2}}\left(\mathcal{S}_L^{+}p_L + \mathcal{S}_R^{-}p_R\right) \end{pmatrix}, \tag{46}$$

where,

$$\mathcal{D}^{\pm}{}_{L,R} = \left[\alpha\left(1+\beta\right) - \beta\mathcal{P}^{\pm}\right]_{L,R}. \tag{47}$$

The pressure splitting coefficient is:

$$\mathcal{P}_{L,R}^{\pm} = \frac{1}{4}\left(M_{L,R} \pm 1\right)^2\left(2 \mp M_{L,R}\right). \tag{48}$$

For the pressure term in the energy equation, the contravariant speed of sound $\overline{C}$ is consistent with $\overline{U}$ and is calculated as:

$$\overline{C} = C - l_t, \quad \text{with} \quad \mathcal{S}^{\pm}{}_{L,R} = \left[\bar{\alpha}^{\pm}\left(1+\bar{\beta}\right)M - \bar{\beta}\bar{M}\right]_{L,R}, \quad \text{and where} \quad \bar{M} = \frac{\overline{U}}{\overline{C}}. \tag{49}$$

$\bar{\alpha}$ and $\bar{\beta}$ are evaluated based on $\bar{M}$ using the formulations given in eq. (45). The use of $\overline{U}$, $\overline{C}$ and $\bar{M}$ in the pressure term for the energy equation is to take into account the grid speed so that the flux will transit from subsonic to supersonic smoothly. When the grid is stationary, $l_t = 0$, $\overline{C} = C$, $\overline{U} = U$.

The LDE scheme can accurately resolve wall boundary layer profiles, capture crisp shock profiles and exact contact surfaces[1] with low diffusion.

VI.B. The Weighted Essentially Non-oscillatory (WENO) Scheme[16]

The fifth-order accurate WENO ($r = 3$) reconstruction of u^L and u^R can be written as

$$u^L_{i+1/2} = \omega_0 q_0 + \omega_1 q_1 + \omega_2 q_2$$

where

$$q_0 = \frac{1}{3}u_{i-2} - \frac{7}{6}u_{i-1} + \frac{11}{6}u_i, \quad q_1 = -\frac{1}{6}u_{i-1} + \frac{5}{6}u_i + \frac{1}{3}u_{i+1}, \quad q_2 = \frac{1}{3}u_i + \frac{5}{6}u_{i+1} - \frac{1}{6}u_{i+2}$$

and

$$\omega_s = \frac{\alpha_s}{\alpha_0 + \cdots + \alpha_{r-1}}, \quad \alpha_s = \frac{C_s}{\varepsilon + IS_s}, \quad k = 0, \cdots, r-1, \quad C_0 = 0.1, \quad C_1 = 0.6, \quad C_2 = 0.3,$$

$$IS_0 = \frac{13}{12}(u_{i-2} - 2u_{i-1} + u_i)^2 + \frac{1}{4}(u_{i-2} - 4u_{i-1} + 3u_i)^2,$$

$$IS_1 = \frac{13}{12}(u_{i-1} - 2u_i + u_{i+1})^2 + \frac{1}{4}(u_{i+1} - u_{i-1})^2,$$

and

$$IS_2 = \frac{13}{12}(u_i - 2u_{i+1} + u_{i+2})^2 + \frac{1}{4}(3u_i - 4u_{i+1} + u_{i+2})^2$$

where, $\varepsilon = 10^{-2}$ is used following the recommendation in Shen, Wang, and Zha.[17] The u^R is reconstructed following the symmetry rule as that to the u^L at interface $i + 1/2$. In this paper, the WENO scheme described above is used to evaluate the conservative variables with 5th order accuracy. The interface flux is then approximated with 5th order accuracy based on the approximate Riemann solver of the implicit flux.

VII. The Discretization of Viscous Terms

A fully conservative fourth-order accurate finite central differencing scheme developed in[18,19] is employed for the viscous terms. For examples

$$\frac{\partial R}{\partial \xi}|_i = \tilde{R}_{i+1/2} - \tilde{R}_{i-1/2}, \quad \text{where} \tag{50}$$

$$\tilde{R}_{i-1/2} = \frac{1}{24\Delta\xi}(-R_{i+1/2} + 26R_{i-1/2} - R_{i-3/2}), \quad R_{i-1/2} = [(\xi_x \tau_{xx}) + (\eta_y \tau_{xy}) + (\zeta_z \tau_{xz})]_{i-1/2}\,, \tag{51}$$

$$\begin{aligned} \text{and} \quad (\tau_{xx})_{i-1/2} = \quad & \mu|_{i-1/2}\{\tfrac{4}{3}\left[(\xi_x \tfrac{\partial u}{\partial \xi})|_{i-1/2} + (\eta_x \tfrac{\partial u}{\partial \eta})|_{i-1/2} + (\zeta_x \tfrac{\partial u}{\partial \zeta})|_{i-1/2}\right] \\ & -\tfrac{2}{3}[(\xi_y \tfrac{\partial v}{\partial \xi})|_{i-1/2} + (\eta_y \tfrac{\partial v}{\partial \eta})|_{i-1/2} + (\zeta_y \tfrac{\partial v}{\partial \zeta})|_{i-1/2} \\ & (\xi_z \tfrac{\partial w}{\partial \xi})|_{i-1/2} + (\eta_z \tfrac{\partial w}{\partial \eta})|_{i-1/2} + (\zeta_z \tfrac{\partial w}{\partial \zeta})|_{i-1/2}]\} \end{aligned} \tag{52}$$

To achieve strict 4th-order accuracy, Eqs.(51)-(52) must be used. For interface $I = i - 3/2, i - 1/2, i + 1/2$, the following formulas must be adopted.

$$\mu_I = \sum_{l=m}^{n} C^I_l \mu_{i+l}, \ m = -2, n = 1, \qquad \frac{\partial u}{\partial \xi}|_I = \frac{1}{\Delta\xi}\sum_{l=r}^{s} D^I_l u_{i+l}, \ r = -3, n = 2, \tag{53}$$

$$\frac{\partial u}{\partial \eta}|_I = \sum_{l=m}^{n} C_l^I \frac{\partial u}{\partial \eta}|_{i+l,j}, \ m=-2, n=1, \quad \text{and} \quad \frac{\partial u}{\partial \eta}|_{i,j} = \frac{1}{\Delta \eta}\sum_{l=p}^{q} C_l^c u_{i,j+l}, \ p=-2, q=2. \tag{54}$$

The other terms are determined similarly. By choosing different ranges for $(m,n), (r,s), (p,q)$ and different coefficients C_l^I, D_l^I, C_l^c, one can obtain the different order accuracy of the viscous terms. In this paper, we take $(m,n) = (-2,1), (r,s) = (-3,2), and\ (p,q) = (-2,2)$, then μ_I, $\frac{\partial u}{\partial \eta}|_I$, $\frac{\partial u}{\partial \eta}|_{i,j}$ achieve fourth-order accuracy, and $\frac{\partial u}{\partial \xi}|_I$ achieve fifth-order accuracy.[18] The coefficients C_l^I, D_l^I, C_l^c are given in Tables 1-3.

Table 1. The coefficients of C_l^I

I	C_{-2}^I	C_{-1}^I	C_0^I	C_1^I
$i-3/2$	5/16	15/16	-5/16	1/16
$i-1/2$	-1/16	9/16	9/16	-1/16
$i+1/2$	1/16	-5/16	15/16	5/16

Table 2. The coefficients of D_l^I

I	D_{-3}^I	D_{-2}^I	D_{-1}^I	D_0^I	D_1^I	D_2^I
$i-3/2$	71/1920	-141/128	69/64	1/192	-3/128	3/640
$i-1/2$	-3/640	25/384	-75/64	75/64	-25/384	3/640
$i+1/2$	-3/640	3/128	-1/192	-69/64	141/128	-71/1920

Table 3. The coefficients of C_l^c

C_{-2}^c	C_{-1}^c	C_0^c	C_1^c	C_2^c
1/12	-8/12	0	8/12	-1/12

VII.A. Implicit Time Integration

In the current work, the finite difference method is used to discretize the governing equations for a steady state solution. To achieve high convergence rate, the implicit time marching scheme is used with the unfactored Gauss-Seidel line relaxation. To enhance diagonal dominance, the first order Euler method is used to discretize the temporal term

$$\begin{aligned} &\tfrac{\Delta V}{\Delta t}\left(Q^{n+1}-Q^n\right) + \left(E_{i+\frac{1}{2}} - E_{i-\frac{1}{2}}\right)^{n+1} + \left(F_{j+\frac{1}{2}} - F_{j-\frac{1}{2}}\right)^{n+1} + \left(G_{k+\frac{1}{2}} - G_{k-\frac{1}{2}}\right)^{n+1} \\ &\quad = \tfrac{1}{Re}\left[\left(R_{i+\frac{1}{2}} - R_{i-\frac{1}{2}}\right)^{n+1} + \left(S_{j+\frac{1}{2}} - S_{j-\frac{1}{2}}\right)^{n+1} + \left(T_{k+\frac{1}{2}} - T_{k-\frac{1}{2}}\right)^{n+1} + D^n \Delta V\right] + S_{MHD}^n \Delta V. \end{aligned} \tag{55}$$

where n and $n+1$ are two sequential time levels with a time interval of Δt. A first-order Taylor expansion for the $n+1$ time level is used for all inviscid and viscous terms above. The discretized equations are given as the following

$$\begin{aligned}&\Delta Q^{n+1}_{i,j,k} + A^{+}\Delta Q^{n+1}_{i+1,j,k} + A\Delta Q^{n+1}_{i,j,k} + A^{-}\Delta Q^{n+1}_{i-1,j,k} + B^{+}\Delta Q^{n+1}_{i,j+1,k} + B\Delta Q^{n+1}_{i,j,k}\\ &+B^{-}\Delta Q^{n+1}_{i,j-1,k} + C^{+}\Delta Q^{n+1}_{i,j,k+1} + C\Delta Q^{n+1}_{i,j,k} + C^{-}\Delta Q^{n+1}_{i,j,k-1} = RHS^{n},\end{aligned} \tag{56}$$

where RHS^n is the summation of all the terms on the right hand side (RHS) of the equation, and

$$\begin{aligned}RHS^{n} = \tfrac{\Delta t}{Re\Delta V}&\left\{\left[\left(R^{n}_{i+\frac{1}{2}} - R^{n}_{i-\frac{1}{2}}\right) + \left(S^{n}_{j+\frac{1}{2}} - S^{n}_{j-\frac{1}{2}}\right) + \left(T^{n}_{k+\frac{1}{2}} - T^{n}_{k-\frac{1}{2}}\right)\right]\right.\\ &\left.- \left[\left(E^{n}_{i+\frac{1}{2}} - E^{n}_{i-\frac{1}{2}}\right) + \left(F^{n}_{j+\frac{1}{2}} - F^{n}_{j-\frac{1}{2}}\right) + \left(G^{n}_{k+\frac{1}{2}} - G^{n}_{k-\frac{1}{2}}\right)\right]\right\} + \tfrac{1}{Re}D^{n}\Delta t + S^{n}_{MHD}\Delta t.\end{aligned} \tag{57}$$

The Gauss-Seidel line relaxation is applied on each direction respectively and is swept forward and backward once within each physical time. For example, if the sweeping is in the i direction from smaller index to larger one, Eq. [56] will be

$$B^{-}\Delta Q^{n+1}_{i,j-1,k} + \bar{B}\Delta Q^{n+1}_{i,j,k} + B^{+}\Delta Q^{n+1}_{i,j+1,k} = RHS' \tag{58}$$

where, $\bar{B} = I + A + B + C$. The terms in the neighboring cells in the i and k directions are absorbed into RHS^n as RHS',

$$RHS' = RHS^{n} - A^{+}\Delta Q^{n}_{i+1,j,k} - A^{-}\Delta Q^{n+1}_{i-1,j,k} - C^{+}\Delta Q^{n}_{i,j,k+1} - C^{-}\Delta Q^{n+1}_{i,j,k-1} \tag{59}$$

The unfactored implicit Gauss-Seidel line relaxation employed in this paper is significantly more efficient than the LU-SGS implicit scheme.[20]

VIII. Mach 10 equilibrium and chemically frozen 3D MHD flow over hemispherical blunt body

We present our results for Mach 10 hypersonic flow around a hemispherical blunt body for both chemically frozen and chemical equilibrium air at an altitude of 60 km. The hemisphere has a radius of 1 cm, the same as in the paper by Damevin and Hoffmann.[21] Our simulations use a 1st order MUSCL scheme combined with van Leer flux vector splitting on the implicit left hand side. On the right hand side we apply the 5th order WENO E-CUSP scheme. The reader should notice that in our formulation the so called RHS contains both inviscid and viscous fluxes. We have studied Mach 5 flow under the same conditions and we have found that there is not much difference between the behavior of chemically frozen and chemical equilibrium air, and that the temperature does not rise enough to produce a significant electrical conductivity.The left panel of Fig. [1] shows the 3D grid used for the hemispherical blunt body. The outer region is divided into 32 blocks of 64x64x4 x-y-z cells each that go to 32 processors. The inner region at the tip of the body, shown magnified in the right panel, is divided into 4 blocks of 64x16x16 cells each that go to 4 processors. Figs. [2] and Fig. [3] compare the the chemically frozen air pressure and temperature along the stagnation streamline, and along a radial line at 45° from the flow direction for different grid densities. The results agree very well, and we have settled on the grid of Fig. [1] for the the presentation of our other results. The simulation parameters correspond to an altitude of 60 km, with a temperature $T_\infty = 247$ K, pressure $p_\infty = 21.96$ Pa, density $\rho_\infty = 3.097 \times 10^{-4}$ kg/m^3,

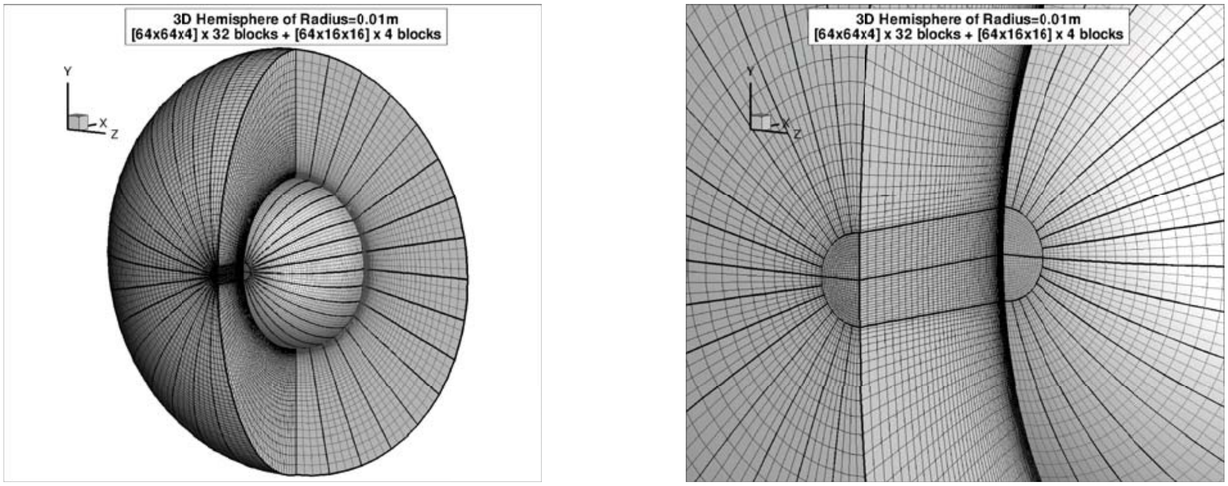

Figure 1. Views of the grid for the symmetric blunt body. Axes in meters.

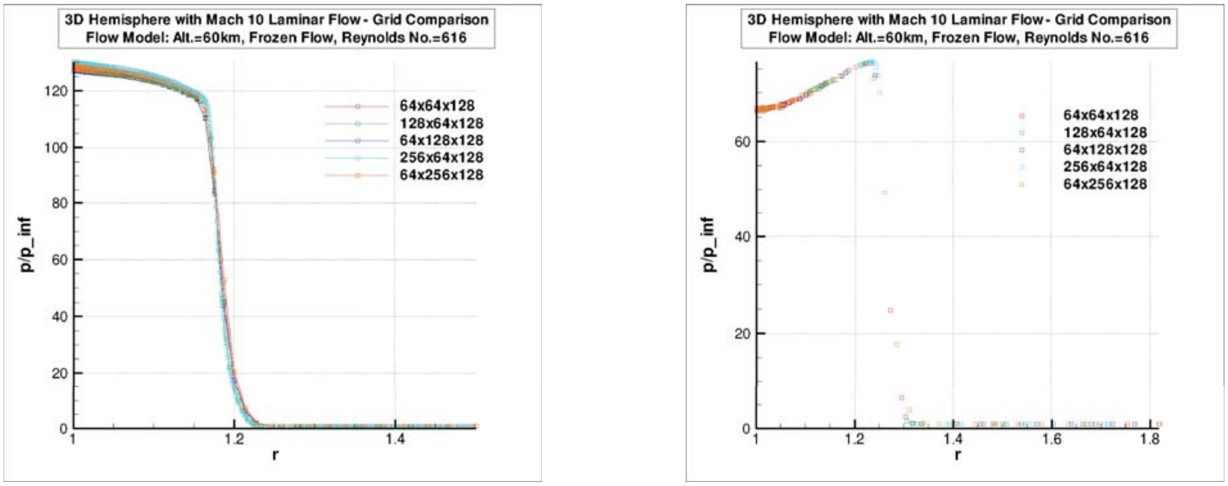

Figure 2. Frozen air pressure profiles for different grid densities. The left panel along the stagnation streamline and the right panel along a radial line at 45° from the flow direction.

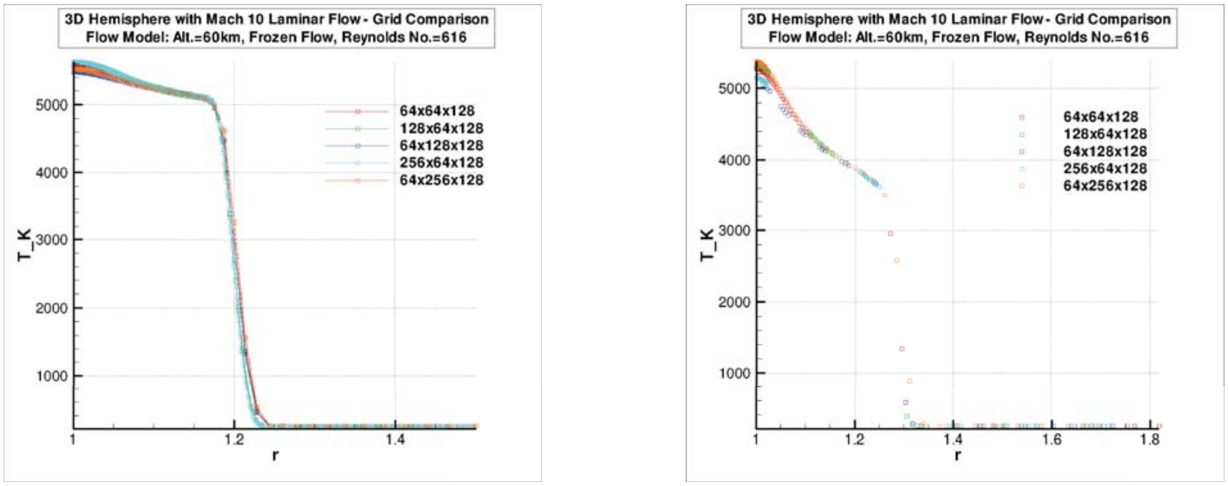

Figure 3. Frozen air temperature profiles for different grid densities. The left panel along the stagnation streamline and the right panel along a radial line at 45° from the flow direction.

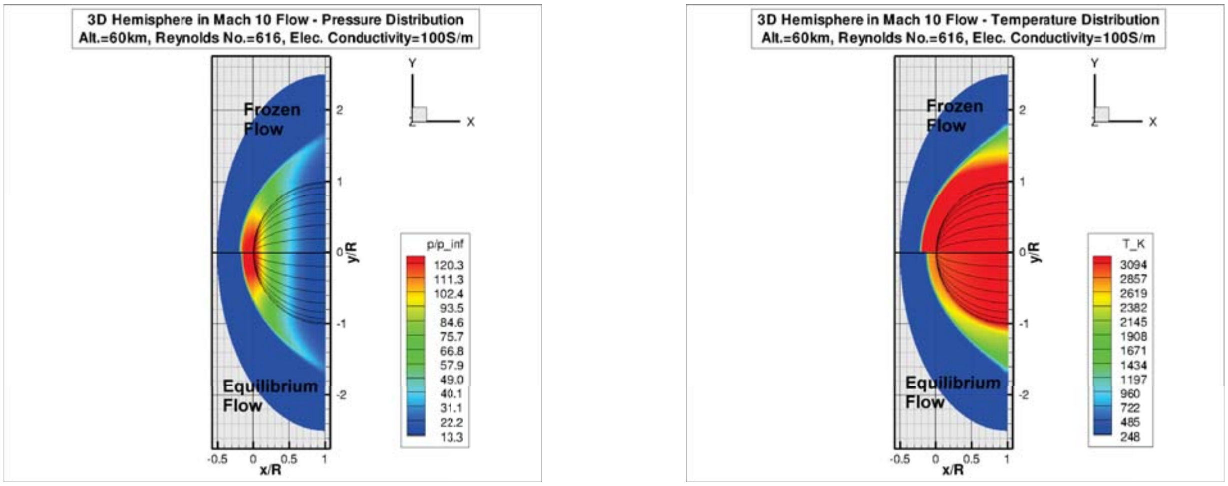

Figure 4. Comparison of pressure and temperature fields for chemically frozen and equilibrium air.

molecular Prandtl number 0.71, and Reynolds number $R = 616$. The speed of sound at infinity is $a_\infty = 315.1$ m/s. Due to the low Reynolds number we use the laminar Navier - Stokes equation and Sutherland's law for the viscosity, which gives $\eta = 1.584 \times 10^{-5}$ Pa·s. The temperature obeys the adiabatic B. C. on the surface of the body. We imitate the effects of the Mach 10 shock on the electrical conductivity by simply turning on the value $\sigma = 100$ Siemen/m in the flow region where the temperature is above 4000 K, and zero elsewhere, which seems a fair approximation to the real situation. This gives a magnetic Reynolds number $Re_m = 3.96 \times 10^{-3}$. In Fig. [4], which is split top and bottom, the left panel shows the pressure fields for frozen and equilibrium flows with no magnetic field. The main difference is that the shock standoff distance is larger in the frozen flow. The right panel shows the temperature fields. Here it is clear that the temperature field around the body is considerably lower with equilibrium air, as expected because of molecular dissociation, vibration, ionization, etc. It can be seen that the hottest temperature with frozen flow begins at the stagnation point and occupies a large region around the body, while with equilibrium flow the hottest temperature occurs in a very thin region around the body. Fig.

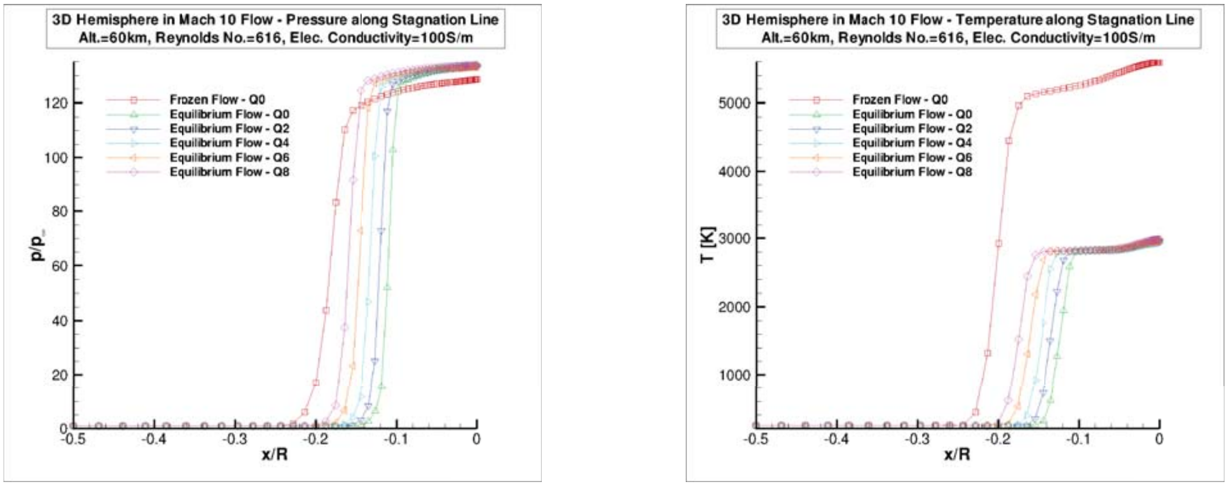

Figure 5. Stagnation streamline pressure and temperature for frozen and equilibrium air with $Q = 0, 2, 4, 6, 8$.

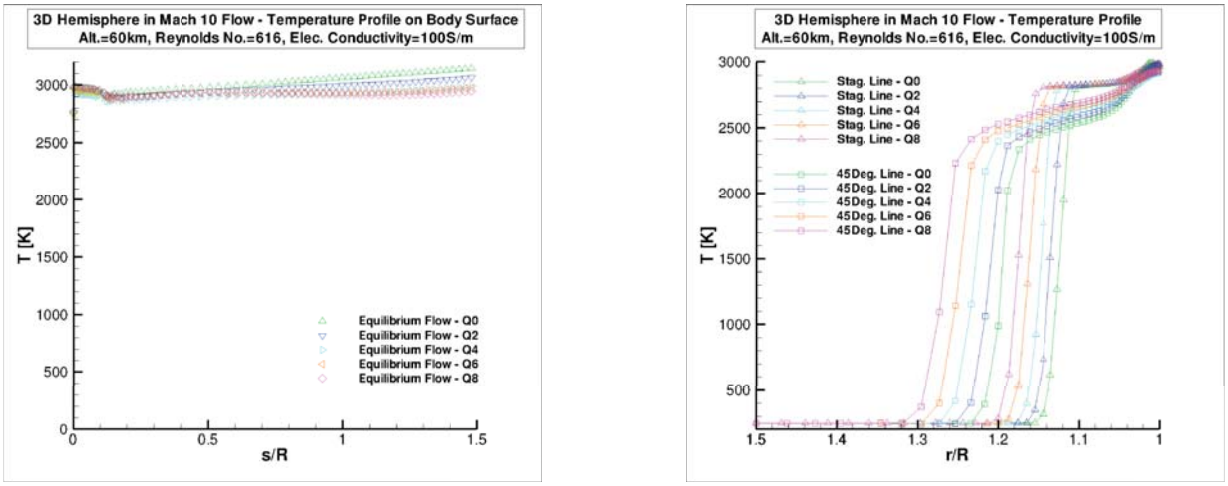

Figure 6. Temperature for equilibrium air with $Q = 0, 2, 4, 6, 8$ along the body surface, the stagnation line and a 45° line.

[5] shows the pressure and temperature profiles along the stagnation streamline for frozen and equilibrium flows at $B = 0$, and for several values of the magnetic interaction parameter $Q = \sigma_e B^2 L_\infty / \rho U_{ref}$ in equilibrium flows. The magnetic field is applied by a point dipole at the center of the hemisphere. The magnetic field strengths used occur at the front tip of the body. Under our conditions, the values $Q = 2$, and 4 correspond very nearly to $B = 1$ and 2 T. Fig. [5] shows that there is a reduction in temperature of almost 2,000 K due to real gas effects, and that the shock standoff distance is reduced by real air effects, but increases almost linearly with Q.The left panel shows that magnetic field increases the shock standoff distance slightly. The right panel shows that the temperature on the body surface is somewhat reduced by the magnetic field. For example, on the tip of the body is $T = 2944$ K for $Q = 0$ and 2904 for $Q = 8$, and at the rear of the body is $T = 3170$ for $Q = 0$ and 2985 for $Q = 8$. The left panel of Fig. [6] shows the temperature variation versus s/R, where s is arc length along the body surface in the flow direction. It shows a decrease of about 10% in the temperature toward the rear ($s \approx 1.5R \approx 1.5\ rmcm$) as the magnetic field is increased from 1T to about 2.8 T. The right panel of Fig. [6] shows the temperature variation along the stagnation line and along a radial line at 45° starting at the body, where $r = R$ and going outward past the position of the shock. It shows that the magnetic field increases the temperature behind the shock and also increases the distance from the body to the shock. The two panels of Fig. [7], which are split top and bottom, compare the pressure and temperature fields for chemical equilibrium air with $Q = 0$ and $Q = 8$.

IX. Validation of computer code

We validate our simulations by comparing with the results of Damevin and Hoffmann[21] for 3D Mach 5 flow of frozen and equilibrium air at an altitude of 40 km. We use the same body as in Ref. [21], which is the same as that in Sec. VIII. We have compared our results using 3rd and 5th order WENO schemes, and we find that the agreement with Ref. [21] is better with 5th order WENO. Fig. [8] we show our results with zero magnetic field for the pressure and temperature profiles along the stagnation streamline for both frozen and equilibrium flows using the 5th order WENO scheme. The left panel indicates the value of

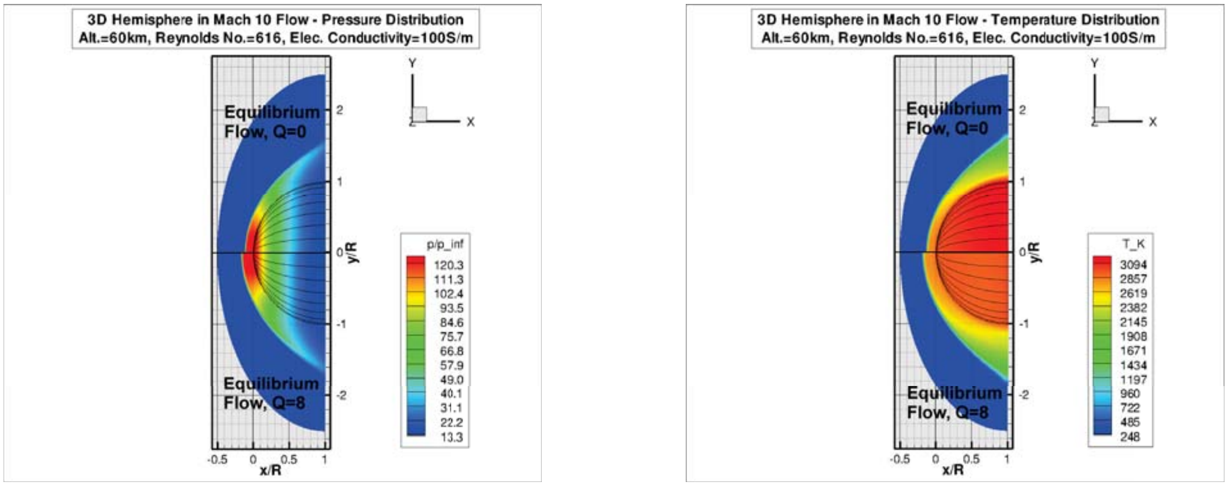

Figure 7. Comparison of pressure and temperature fields for equilibrium air with $B = 0$ T and $B = 2$ T.

the shock standoff distance in the two cases. These profiles agree very well with Fig. [8] of Ref. [21]. The shock standoff distances also agree with the values shown in Fig. [7] of Ref. [21].

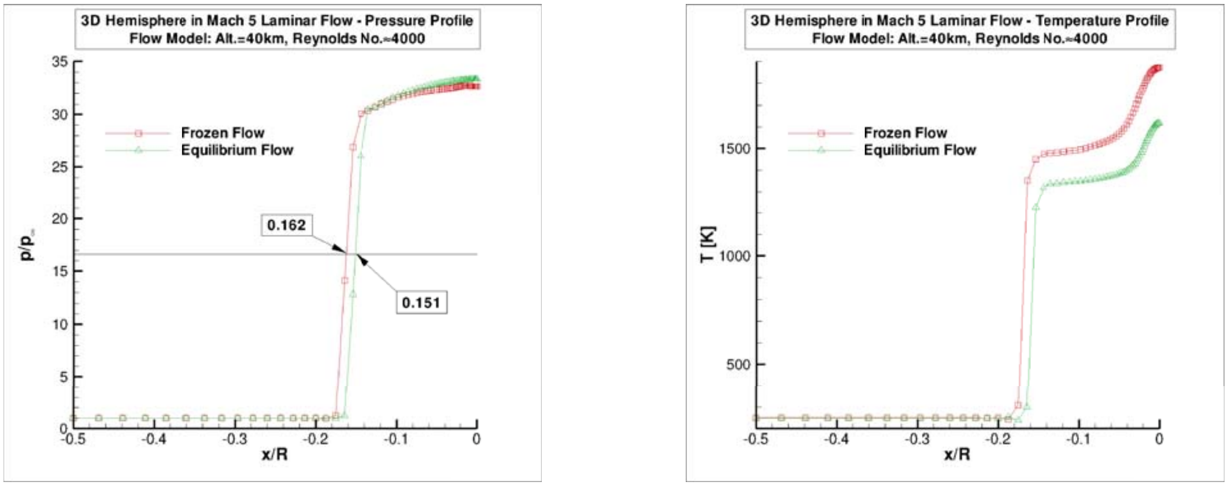

Figure 8. Mach 5 validation Pressure and temperature profiles along stagnation streamline.

X. Conclusions and Future Work

We have succeeded in incorporating the low magnetic Reynolds number MHD model and real gas effects into the low diffusion E-CUSP (LDE) scheme with a fifth order WENO scheme recently developed by Zha[1] et al. The fact that the physical effects that we have found in our simulations are well known and have have been found before by the authors already cited, and the agreement seen in of our validation runs, give us confidence in our method. We are planning to have results with nonequilibrium air, and a realistic electrical conductivity in future work, as well as calculating the reaction force due to the integral of $\mathbf{J} \times \mathbf{B}$ over the fluid volume.

Acknowledgments

This work was supported in part by the U. S. Air Force Office of Scientific Research under Grants FA9550-09-1-0105 monitored by Dr. Robert Barker, and FA49620-03-1-0253 monitored by Dr.Fariba Fahroo. We also acknowledge the valuable assistance of Dr. Yiqing Shen.

References

[1] Zha, G.-C., Shen, Y., and Wang, B., "Calculation of Transonic Flows Using WENO Method with a Low Diffusion E-CUSP Upwind Scheme," AIAA Paper 2008-0745, 46th AIAA Aerospace Sciences Meeting, Reno, NV, Jan. 2008.

[2] Lee, J., Huerta, M., and Zha, G., "3D Steady Hypersonic Laminar Flow Using High Order WENO Schemes," AIAA Paper 2009-3913, 2009.

[3] Bityurin, V. A., Lineberry, J. T., Potebnia, V. G., Alferov, V. I., Kuranov, A. L., and Sheikin, E. G., "Assessment of Hypersonic MHD Concepts," AIAA Paper 97-2393, 1997.

[4] Bityurin, V. A. and Bocharov, A. N., "Effects of MHD Interaction in Reentry Flight," AIAA Paper 2006-3235, 2006.

[5] Zeigarnik, V. A. B. V. A., , and Kuranov, A. L., "On a Perspective of MHD Technology in Aerospace Applications," AIAA Paper 1996-2355, 1996.

[6] Fujino, T., Kon, S., and Ishikawa, M., "Preliminary Analysis of Electric Power Extraction by MHD Technology in Reentry Flight," AIAA Paper 2007-4248, 2007.

[7] MacCormack, R. W., "Simulation of Hypersonic Flow within a Strong Magnetic Field," AIAA Paper 2007-397, 2007.

[8] Hoffmann, K. A., Damevin, H. M., and Dietiker, J., "Numerical Simulation of Hypersonic NUumber Magnetofluiddynamic Flows," AIAA Paper 2000-2259, 2000.

[9] Srinivasan, S., Tannehill, J. C., and Weilmuenster, K. J., "Simplified Curve Fits for the Thermodynamic Properties of Equilibrium Air," NASA Reference Publication 1181 August 1987, 1987.

[10] Srinivasan, S., Tannehill, J. C., and Weilmuenster, K. J., "Simplified Curve Fits for the Thermodynamic Properties of Equilibrium Air," ISU-ERI-Ames-86401 (Grant NAG-1-313), Engineering research Inst., Iowa State Univ. June 1986, 1986.

[11] MacCormack, R. W., "Flow Simulations within Strong Magnetic Fields," AIAA Paper 2008-1070, 2008.

[12] Khan, O. U., Hoffmann, K. A., and Dietiker, J., "Validity of Low Magnetic Reynolds NUumber Formulation of Magnetofluiddynamics," AIAA Paper 2007-4374, 2007.

[13] Tomoyuki, Y., Takayasu, F., and Ishikawa, M., "Numerical Analysis of Reentry Trajectory Coupled with MHD Flow Control," AIAA Paper 2007-4249, 2007.

[14] Edwards, J. R., "A Low-Diffusion Flux-Splitting Scheme for Navier-Stokes Calculations," AIAA Paper 95-1703-CP, June, 1995.

[15] Edwards, J. R., "A Low-Diffusion Flux-Splitting Scheme for Navier-Stokes Calculations," *Computer & Fluids*, Vol. 6, 1997, pp. 635–659.

[16] Shu, C.-W., "Essentially Non-Oscillatory and Weighted Essentially Non-Oscillatory Schemes for Hyperbolic Conservation Laws," NASA /CR-97-206253, ICASE Report NO.97-65, 1997.

[17] Shen, Y.-Q., Wang, B.-Y., and Zha, G.-C., "Applications of Implicit WENO Scheme for Compressible Flows ," AIAA Paper 2007-4431, 2007.

[18] Shen, Y., Wang, B., and Zha, G., "Implicit WENO Scheme and High Order Viscous Formulas for Compressible Flows," AIAA Paper 2007-4431, 2007.

[19] Shen, Y., Zha, G., and Chen, X., "High Order Conservative Differencing for Viscous Terms and the Application to Vortex-Induced Vibration Flows," AIAA Paper 2008-4059, 2007.

[20] Shen, Y.-Q. and Zha, G.-C., "A Comparison Study of Gauss-Seidel Iteration Methods for Internal and External Flows," AIAA Paper 2007-4332, 2007.

[21] Damevin, H. M. and Hoffmann, K. A., "Numerical Simulations of Hypersonic Magnetogasdynamic Flows Over Blunt Bodies," AIAA Paper 2002-0201, 2002.